Self-optimizing Cobalt Tungsten Oxide Electrocatalysts toward Enhanced Oxygen Evolution in Alkaline Media

Christean Nickel,[a] David Leander Troglauer,[a] Zsolt Dallos,[a] Dhouha Abid,[a] Kevin Sowa,[a] Magdalena Ola Cichocka,[b] Ute Kolb,[a, b] Boris Mashtakov,[a] Shikang Han,[a] Lijie Ci,[c] Deping Li,[c] Xiaohang Lin,[d] Minghao Hua,[e,*] Rongji Liu,[a,*] Dandan Gao[a,*]

[a] Department of Chemistry, Johannes Gutenberg University Mainz, Duesbergweg 10-14, Mainz 55128, Germany
[b] Research Division of Electron Crystallography, Technical University of Darmstadt, Schnittspahnstr. 9, 64287 Darmstadt, Germany
[c] State Key Laboratory of Advanced Welding and Joining, School of Materials Science and Engineering, Harbin Institute of Technology (Shenzhen), Shenzhen 518055, People's Republic of China
[d] Key Laboratory for Liquid-Solid Structural Evolution and Processing of Materials, Ministry of Education, School of Materials Science and Engineering, Shandong University, Jinan 250061, People's Republic of China
[e] School of Energy and Power Engineering, Shandong University, Jinan 250061, People's Republic of China

Emails: huaminghao@mail.sdu.edu.cn, rongji.liu@uni-mainz.de, dandan.gao@uni-mainz.de

Abstract: Self-optimizing mixed metal oxides are a novel class of electrocatalysts for the advanced oxygen evolution reaction (OER). Here, we report the self-assembled cobalt and tungsten oxide nanostructures on the lab-synthesized copper oxide substrate via a one-step deposition approach. The resulting composite demonstrates remarkable self-optimization, achieving significantly reduced overpotentials and enhanced current densities. Mechanistic investigations reveal the origins of the boosted OER performance, highlighting substantial enhancements in OER kinetics, the electrocatalytically active surface area, surface wettability, and electrical conductivity. Interfacial restructuring of the electrocatalyst under operating conditions indicates the in situ formation of oxidized cobalt species as true active sites. Complementary density functional theory (DFT) analysis demonstrates the formation of *OOH as the rate-determining step of OER, and elucidates the self-activation mechanism originating from the adaptation of adsorbed oxygen intermediates binding site from tungsten to cobalt. Our study provides a fundamental understanding of the self-optimization mechanism and advances the knowledge-driven design of efficient water-splitting electrocatalysts.

Keywords: electrocatalysis, metal oxides, self-optimization, oxygen evolution reaction, active sites

Introduction:

The electrochemical splitting of water into hydrogen and oxygen is a pivotal process for achieving carbon-neutral energy production. When coupled with renewably “green” electricity sources, this approach can form the basis of a fully sustainable energy scheme.[1,2] However, significant challenges remain, including the highly oxidative conditions, slow kinetics of proton-coupled multielectron transfer, and substantial energetic activation barriers associated with the indispensable oxygen evolution reaction (OER).[3–5] Traditionally, noble metal oxides such as RuO_2[6] and IrO_2,[7] known for their high activity toward OER, have been the benchmark electrocatalysts. Nevertheless, the large-scale use of these materials is severely hindered by their rarity, high cost, and susceptibility to degradation in both acidic and alkaline environments.[8]

In response to the demand for more sustainable electrocatalysts, research has increasingly focused on the development of industrially viable alternatives based on inexpensive earth-abundant metal compounds. Notably, 3d to 5d transition metal oxides, particularly those incorporating Co, Ni, Fe, Cu and W,[9–13] have garnered significant attention due to their impressive catalytic activity and robust long-term durability, especially when formulated as mixed metal (*e.g.*, Ni-Co,[14,15] Ni-Fe,[15] Co-Fe,[16,17] Cu-Co,[18,19] Cu-W,[20] Ni-W,[21,22] Fe-W,[23] Co-W,[24] Fe-Ni-W,[25] Co-Ni-Fe,[26] Co-Ni-W,[27] Co-Fe-W,[28,29] Co-Cu-W[30,31]) oxides. In this regard, the underlying synergistic effects within these mixed metal oxides are critical for improving the OER performance grounded on enriched reaction active sites, boosted chemical / structural stability, or optimized electronic structures,[32–36]

thereby enabling more efficient water splitting processes.

In particular, self-optimizing mixed metal oxides have been recognized as a novel class of OER electrocatalysts, characterized by progressively enhanced performance during operation. For example, Yamada et al. synthesized a tetravalent perovskite oxide, $CaFe_{0.5}Co_{0.5}O_3$, demonstrating enhanced OER activity over 100 cyclic voltammetry (CV) tests attributed to the smaller charge-transfer energies and formation of mixed Fe^{4+} / Co^{4+} active sites.[37] In another example, Nguyen et al. developed a tungsten-doped cobalt oxide film electrocatalyst that exhibited improved OER activity and kinetics, arising from enhanced surface wettability and increased electrochemically active surface area (ECSA) under O_2-evolving potentials.[38] Recently, some of us have previously used molecular metal oxides (polyoxometalates, POMs) as well-defined single-source-precursors for OER electrocatalysts, where cobalt-functionalized polyoxotungstate ($[Co^{II}_4(H_2O)_2(PW_9O_{34})_2]^{10-}$, Co_4POM) was immobilized on commercial TiO_2 using the cationic polymer polyethylenimine (PEI) as a linking agent.[39] The resulting composite OER electrocatalyst demonstrated a unique self-activation behavior, owing to the re-structuring of Co_4POM pre-electrocatalyst. This led to the in situ formation of highly active Co^{III} oxide and/or hydroxide moieties, which was accompanied by an increase in both electrical conductivity and ECSA.

Despite their promotion of sustainable OER, the design of desired catalysts capable of enhanced OER electrocatalysis is still in its infancy. Moreover, the chemical adaptations during the self-optimization involving surface restructuring, generation of new phases and alteration of metal oxidation state is largely unknown.[40] To address these critical challenges, advances in experimental and computational electrochemical surface analyses are urgently required to reveal the self-optimization mechanism and therefore drive the knowledge-based design of next-generation self-optimizing OER electrocatalysts.[41,42] Furthermore, the development of viable and scalable deposition approaches is of utmost technological, economic and ecological significance, enabling stable anchoring of OER pre-catalysts on selected substrates with high mechanical integrity.[43]

In this work, we report a facile one-step robust deposition of self-assembled mixed Co-W oxides on lab-synthesized CuO microflower substrate using varying Co^{2+} / $[SiW_{11}O_{39}]^{8-}$ precursor molar ratios of 1 : 1 (composite **1**), 2 : 1 (composite **2**), 3 : 1 (composite **3**) and 4 : 1 (composite **4**), respectively. When operated in 1.0 M aqueous KOH, the resulting composite **3** exhibits a most remarkably self-optimizing catalytic performance with progressively decreased overpotentials and Tafel slopes, as well as increased maximum current densities, ECSA, surface wettability and electrical conductivity. Explicitly, post-catalytic X-ray photoelectron spectroscopy (XPS) proved the oxidized valence state of the Co and W metal center. Furthermore, OER process-dependent attenuated total reflection Fourier transform infrared (ATR-FTIR) spectroscopy and Raman spectroscopy measurements revealed the dynamic interfacial processes / surface restructuring that governs boosted catalytic performance at a molecular level. In addition, DFT calculation unraveled that the formation of *OOH as the rate-determining step of OER and proved that composite **3** after self-optimization exhibits a lower OER overpotential and higher electrical conductivity for enhanced OER.

This initial proof of concept paves the way for the development of self-assembled proficient electrocatalysts, in which molecular precursors are transformed into self-optimizing nanostructures to promote multi-electron electrocatalysis.

Electrocatalyst fabrication and characterization:

Here, we present a scalable fabrication method for mixed metal oxides through a simple one-pot wet-chemical deposition process (**Fig. 1a**). This approach yields a highly nanostructured composite, which serves as a promising self-optimizing electrocatalyst for enhanced alkaline OER. The electrocatalyst design was grounded in the lab-synthesized CuO documented in our previous work.[44] Corresponding preparation procedures are available in the Supporting Information (SI).

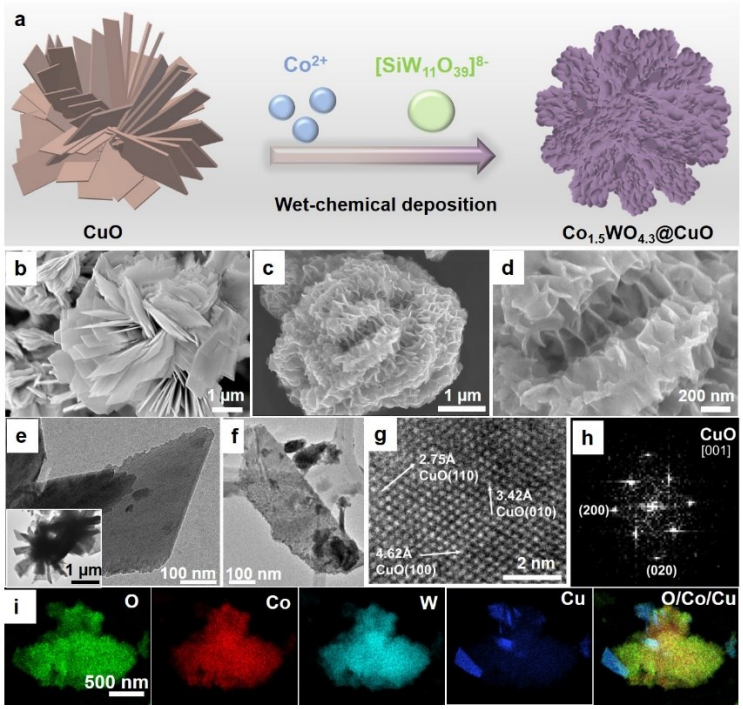

Fig. 1 Synthetic illustration, structural and elemental analysis of as-prepared composite **3**. (a) Schematic materials design and fabrication approach leading to mixed metal oxide composite. (b) SEM image of lab-synthesized CuO, (c-d) SEM images of composite **3**. (e) TEM image of lab-synthesized CuO nanopetal and microflower (inset). (f) TEM image of as-prepared composite **3**. (g) HRTEM and (h) fast Fourier-transformation (FFT) of composite **3**, showing a matching reflection of CuO crystalline substrate. (i) STEM-EDX elemental mappings, showing the elemental distribution of O, Co, W and Cu (for HAADF-STEM image of the particle, see the SI, **Fig. S7**).

As illustrated in scanning electron microscopy (SEM, **Figs 1b** and **S1**) and transmission electron microscopy (TEM, **Fig. 1e** and inset, **Fig. S2**), the lab-synthesized CuO features a flower structure with a diameter of 3 - 5 µm. Energy-dispersive X-ray (EDX) elemental mapping showed a uniform distribution of the constituent Cu and O elements (**Fig. S3**). Powder X-ray diffraction (pXRD, **Fig. S4**) revealed the presence of characteristic crystalline CuO, which is a known semiconductor with high electron mobility[45] and has recently been employed for OER electrocatalysis.[44,46,47] In addition, ATR-FTIR spectroscopy and Raman spectroscopy further identified characteristic Cu-O vibrational modes (**Figs 2e** and **2f**). Subsequent modification of the CuO was achieved by one-step hydrothermal deposition using molecular precursors ($Co(NO_3)_2{\cdot}6H_2O$ and $K_8[SiW_{11}O_{39}]{\cdot}13H_2O$, Co^{2+} / $[SiW_{11}O_{39}]^{8-}$ molar ratio: 3 : 1) at 180 °C for 8 h, leading to the self-assembled Co-W oxide nanostructures rooted on CuO substrate (composite **3**) as demonstrated by SEM (**Figs 1c-d** and **S5**) and TEM (**Fig. 1f**). High-resolution TEM (HRTEM, **Fig. 1g**) and fast Fourier-transformation analysis of the same area (**Fig. 1h**) reveal that the composite **3** is based on CuO crystalline substrate. This observation indicates the amorphous nature of deposited mixed Co-W oxide (**Fig. S6**), which is in accord with the pXRD pattern (**Fig. S12**). In addition, EDX elemental mappings from scanning TEM (STEM) indicate that the deposited catalyst contains O, Co and W, while the presence of Cu nanopetal is assigned to signals arising from the CuO substrate (**Figs 1i** and **S7**).

Further, X-ray photoelectron spectroscopy (XPS) was employed to investigate more detailed chemical structures and the surface oxidation states of composite **3**. The XPS survey spectrum verifies the presence of Co, W, Cu and O (**Fig. S8**). In detail, the Co 2p region reveals the presence of Co^{2+} (**Fig. 2a**), while W 4f region indicates the coexistence of W^{5+} and W^{6+} in a ratio of approximately 1 : 1.3 (**Fig. 2b**).[48] The O 1s region displays three distinct features corresponding to metal-oxygen bonds (M-O, including Co-O, W-O, and Cu-O), hydroxyl groups (O-H), and physically adsorbed water (ad-H_2O), respectively (**Fig. 2c**).[30,49]

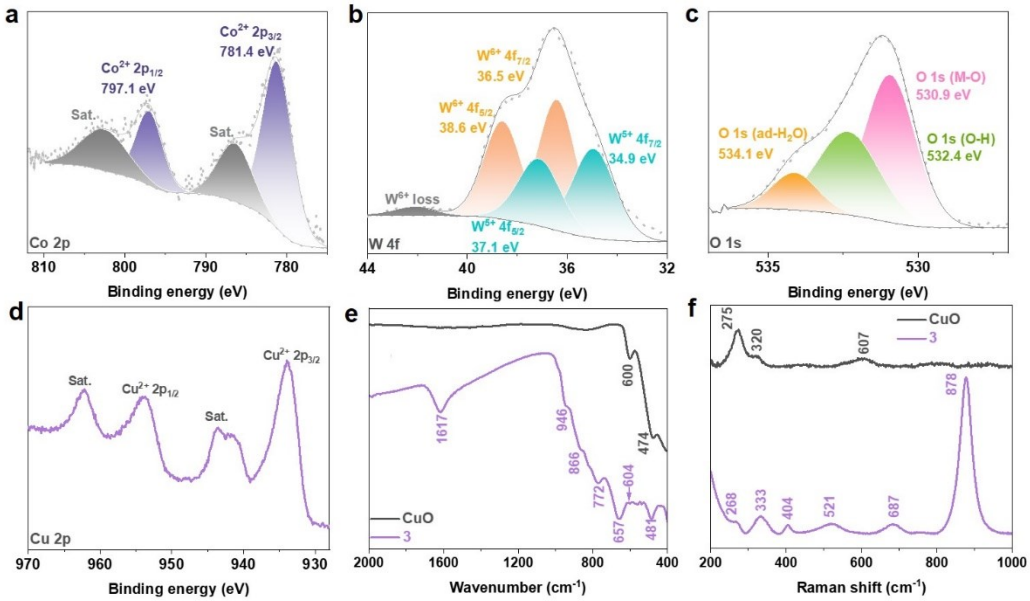

Fig. 2 Deconvoluted XPS spectra for (a) Co 2p, (b) W 4f, (c) O 1s and (d) Cu 2p of composite **3**. (e) ATR-FTIR spectra and (f) Raman spectra of composite **3** and **CuO**.

Additionally, the Cu 2p region confirms the presence of Cu^{2+} originating from the substrate (**Fig. 2d**).[50] The presence of the mixed metal oxide was further corroborated by ATR-FTIR (**Fig. 2e**) and Raman (**Fig. 2f**) spectroscopy. Specifically, the ATR-FTIR spectrum revealed a peak at 946 cm^{-1}, corresponding to the W=O bond, while the peaks at 866 cm^{-1} and 772 cm^{-1} were attributed to W-O-W bonding.[51,52] Additionally, the Co-O vibrational mode was detected at 657 cm^{-1}.[53] The characteristic bands associated with Cu-O were identified at 604 cm^{-1} and 481 cm^{-1},[30] which exhibited a blue shift compared to those of the CuO (600 cm^{-1} and 474 cm^{-1}), suggesting an interaction between Co-W oxide and CuO substrate.[54] Complementarily, the characteristic vibrational modes of composite **3** were also observed in the Raman spectra (W=O: 878 cm^{-1}, W-O-W: 687 cm^{-1}, 333 cm^{-1},[55] Co-O: 521 cm^{-1}, 404 cm^{-1},[30] Cu-O: 268 cm^{-1}[56]). In addition, ATR-FTIR spectroscopy identified O-H vibrations and thermogravimetric analysis (TGA) indicated approximately 6.7 wt-% water of hydration (**Fig. S9**). As measured by inductively coupled plasma optical emission spectroscopy (ICP-OES), the atomic ratio of Co : W in composite **3** is determined to be 1.5 : 1 (**Fig. S10**). In summation, the composite synthesized is best described as a mixed Co-W oxide deposited on CuO with an approximate formula of $Co_{1.5}WO_{4.3}$@CuO · xH_2O.

To assess the role of the Co/W precursors in the synthesis, we performed identical syntheses in varying Co^{2+} / $[SiW_{11}O_{39}]^{8-}$ molar ratios (**Table S1**), namely, 1 : 1 (composite **1**), 2 : 1 (composite **2**), 4 : 1 (composite **4**), as well as in the presence of only Co^{2+} (composite **5**) and $[SiW_{11}O_{39}]^{8-}$ (composite **6**). The resulting composites were used as references to compare the electrocatalytic performance of composite **3**.

Based on the ICP-OES result (**Fig. S10**), the atomic ratio of Co : W in composites **1**, **2** and **4** was revealed to be 0.1 : 1, 0.2 : 1 and 1.9 : 1, respectively. ATR-FTIR data indicate that, in addition to the characteristic Cu-O originating from the substrate, the co-existence of W-O and Co-O vibration modes was observed for composites **2**, **3** and **4** (while it is rather less observable for composite **1**, **Fig. S11a**). As expected, composites **5** and **6** feature Co-O and W-O vibrational modes, respectively (**Fig. S11b**). Furthermore, pXRD data demonstrate that composites **1** and **6** retain the crystallography of CuO substrate, while composites **2** - **4** show reduced crystallinity, and composite **5** is based on newly formed Cu-Co oxide crystalline on CuO substrate (**Fig. S12**).

Moreover, both the Brunauer-Emmett-Teller (BET) specific surface area and the Barrett–Joyner–Halenda (BJH) pore size distribution (**Figs S13**, **S14** and **Table S2**) of composite **3**

showed a considerable increase (18.38 m^2/g and 16.32 nm) compared to the CuO substrate (11.16 m^2/g and 11.42 nm). These enhancements are conducive to improving electrocatalytic OER activity, owing to the increased exposure of active sites and enhanced mass transfer of electrolytes.[18] Interestingly, composites **1** and **2** show relatively lower surface areas in comparison to **3**, while **4** - **6** display unexpectedly lower values than CuO substrate. Moreover, the pore size distribution features dynamic variation. Supplementarily, SEM data of reference composites (**1**, **2**, **4**, **5** and **6**) demonstrate less nanostructured surface morphology compared to **3**, while surface aggregation was observed specifically for **5**, showing the lowest surface area (**Fig. S15** and **Table S2**).

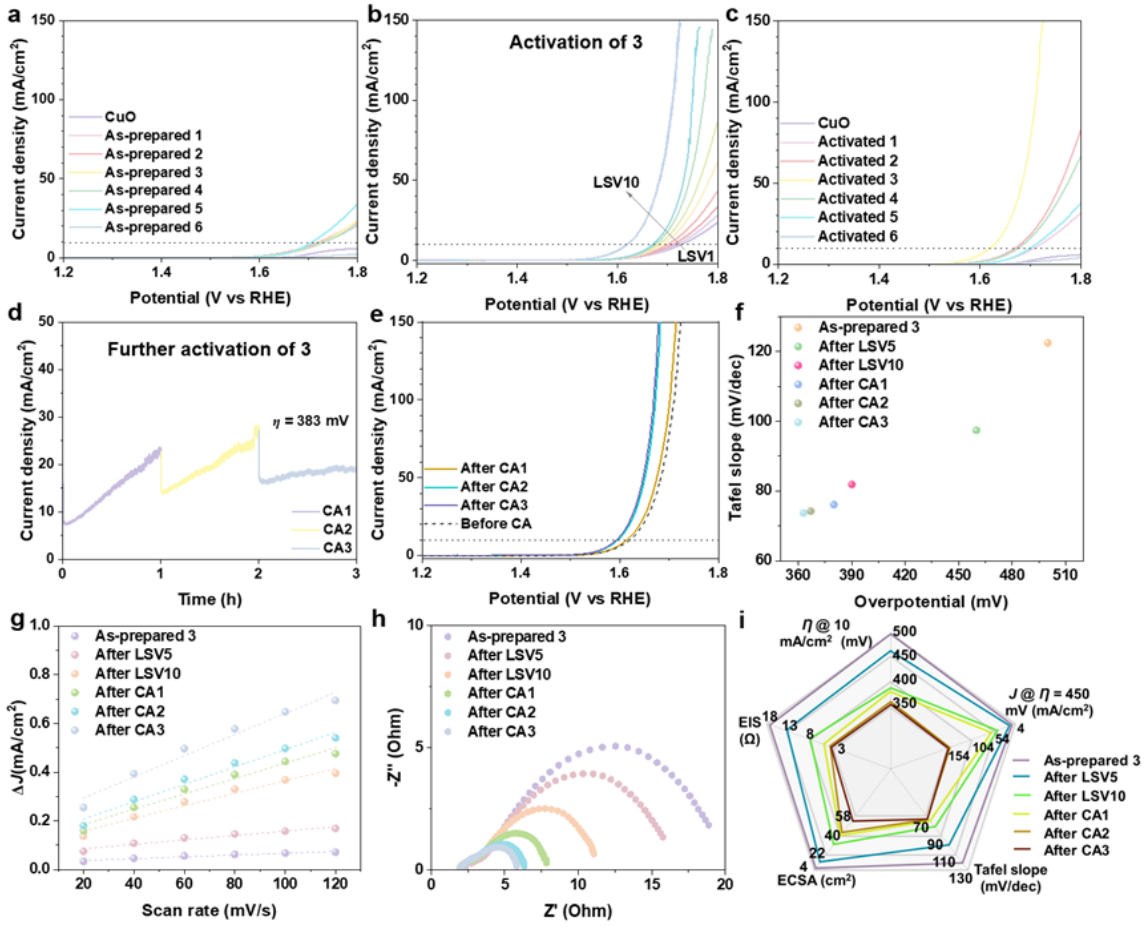

Fig. 3 Electrocatalytic OER performance of composites **1** - **6**, and CuO in 1.0 M aqueous KOH. (a) Initial LSV curves of as-prepared **1** - **6** and CuO (first scan, LSV1). (b) Activation process of **3** by ten successive LSV scans (LSV1 - LSV10). (c) LSV curves of activated **1** - **6** (after respective successive LSV scans) and CuO. (d) Stepped chronoamperometry (CA) test of **3** over a period of 3 h. (e) LSV curves of activated **3** before and after CA tests. (f) Tafel slopes and overpotentials of **3** during the studied OER process. (g) ECSA study of **3**, showing the corresponding linear fits. (h) Electrochemical impedance spectroscopy (Nyquist plots) of **3** measured at the overpotential η = 400 mV. (i) Summary of performance metrics for **3** during the studied OER process.

Electrocatalytic OER performance:

In the next step, we assessed the electrocatalytic OER performance of the mixed metal oxide composites under alkaline media (1.0 M aqueous KOH, pH 13.8, room temperature) using a H-cell with standard three-electrode configuration. All potentials were converted to the reversible hydrogen electrode (RHE) as a reference. The electrocatalytic activity of the as-prepared composites **1** - **6** and CuO was initially evaluated using linear sweep voltammetry (LSV). As illustrated in **Fig. 3a**, the as-synthesized CuO exhibits minimal OER activity. In contrast, composites **1** - **4** demonstrate comparable

behaviors, characterized by increased but still relatively limited OER activity, as well as similar Tafel slopes (**Fig. S16**). Notably, composite **5** shows the highest OER activity and the lowest Tafel slope, whereas composite **6** displays the lowest OER activity with a similar Tafel slope to composites **1** - **4** (**Fig. S16**).

Subsequently, the self-optimization of composites **1** - **6** toward enhanced OER activity was observed by successive LSV scans (**Figs 3b** and **S17a-e**). Specifically, composites **1** and **5** displayed finite self-optimization behavior, reaching stabilized OER activity after 2 and 8 LSV scans, respectively. In contrast, composites **2**, **3**, **4** and **6** demonstrate a more sustained increase in OER activity over 10 LSV scans. Note that, the self-optimization procedure is absent for the lab-synthesized CuO (**Fig. S17f**), underscoring the critical role of the deposited mixed Co-W oxide in enhancing OER performance. The LSV curves for activated composites **1** - **6** and CuO are shown in **Fig. 3c**. Remarkably, activated composite **3** exhibited the lowest onset potential, highest current density and lowest Tafel slope (**Fig. S18a**), attributable to the optimal Co^{2+} / $[SiW_{11}O_{39}]^{8-}$ molar ratio of the precursor solution (**Table S1**). Note that, composites **1** - **4** (Co-W oxide involving), and **6** (W oxide involving) displayed considerably reduced Tafel slope, namely, enhanced OER kinetics while composite **5** (Co oxide involving, W oxide free) showed a marginal decrease in Tafel slope (**Fig. S18b**). This suggests the pivotal role of the W oxides in improving OER kinetics during the successive LSV scanning activation process.

Further self-optimization of **3** was investigated and verified by the stepped chronoamperometry (CA, at overpotential η = 383 mV) over a period of 3 h. As displayed in **Fig. 3d**, a considerable increase in current density was achieved for CA1 (from 7.5 mA/cm^2 to 23.2 mA/cm^2) and CA2 (from 14.0 mA/cm^2 to 27.6 mA/cm^2), while almost stable performance was observed for CA3 (from 16.5 mA/cm^2 to 18.5 mA/cm^2). Correspondingly, the LSV curves (**Fig. 3e**) after CA1 and CA2 demonstrate a further enhancement in OER activity compared to the pre-CA measurements, while maximized OER activity was achieved after CA3, featuring the lowest overpotential η = 363 mV (at J = 10 mA/cm^2) and highest current density of 149.6 mA/cm^2 (at η = 450 mV). In this process, further reduced Tafel slopes (indicative of increased OER kinetics) were also obtained (**Fig. 3f** and **Fig. S19**). The self-optimization process of composite **3** is summarized in **Fig. 3i** and **Table S3**. More intriguingly, the maximum OER activity was maintained over a course of 15 h, despite a noticeable drop in current density during long-term CA, due to the aggregation of O_2 bubbles on the electrode surface that blocked the active sites (**Fig. S20**). For comparison, CA measurement (at η = 570 mV, < 3 h, **Fig. S21a**) was performed for CuO substrate, which however shows degraded OER activity (**Fig. S21b**).

Electrochemical mechanistic studies:

To gain mechanistic insights underlying the unique self-optimization OER process of composite **3**, we conducted further electrochemical analyses to determine the ECSA and the charge-transfer resistance (R_{ct}) at the electrode/electrolyte interface. Specifically, we analyzed the ECSA based on electrochemical double-layer capacitance (C_{dl}) using scan-rate-dependent CV (for details, see **Fig. S22**). As shown in **Figs 3g, 3i**, **S23a** and **Table S3**, continuously rising ECSA (from 4.6 ± 0.4 cm^2 to 54.4 ± 0.4 cm^2) is observed, representing nearly a twelve-fold enhancement after CA3. This significant increase in surface area is attributed to the vigorous formation of O_2 bubbles and the evolution of the electrocatalyst interface, potentially exposing a larger number of accessible active sites contributing to the OER self-optimization process. Complementarily, analysis of the hydrophilicity of the electrode (composite **3** coated carbon paper) surface by the sessile drop method (1.0 M KOH as the medium) showed a gradual decrease in water contact angle (from 122.0 ° to 64.9 °, **Fig. S24**), indicative of increased surface wettability and therefore more sufficient electrolyte-catalyst interface contact. Furthermore, a gradient decrease in R_{ct} (from 17.0 Ω to 3.5 Ω) was revealed by electrochemical impedance spectroscopy (EIS). This suggests that the maximized optimization after CA3, characterized by the lowest R_{ct}, enables the most efficient interfacial electron transfer (**Figs 3h**, **3i**, **S23b**, and **Table 1**). In comparison, the CuO substrate demonstrates substantially lower ECSA (2.7 ± 0.1 cm^2, **Fig. S25**) and markedly higher R_{ct} (191.8 Ω, **Fig. S26**). Overall, composite **3**

exhibits competitive performance in comparison to literature-reported Co-W oxide-based OER electrocatalysts (see **Table S4**), demonstrating comparable or superior metrics after undergoing a unique self-optimization process.

Electrocatalyst interfaces studying:

To elucidate the origins of the self-optimizing behavior of composite **3**, various spectroscopic approaches were used to investigate the electrocatalyst interfaces during the studied OER process. The post-catalytic-XPS analyses uncovered the underlying changes in the chemical composition and oxidation states of the elements. Throughout the studied OER process, the formation of higher oxidized metal species was observed, including the emergence of Co^{3+}[57] with an increased ratio to Co^{2+} (**Fig. S27** and **Table S5**), as well as a rising proportion of W^{6+} compared to W^{5+} (**Fig. S28** and **Table S5**). Notably, after LSV5 and LSV10, the metal-oxygen (M-O) bonds and hydroxyl groups (O-H) remained present in composite **3**, while oxygen atoms in the sulfonic acid group of Nafion were also detected (**Fig. S29**).[58] As the OER process progressed (CA1 - CA3), an increasing proportion of metal-hydroxide (M-OH) and oxyhydroxide (M-OOH) species[59,60] to metal-oxygen (M-O) species (SI, **Table S5**) were observed.

In addition, the OER-process-dependent ATR-FTIR spectra of composite **3** (after LSV5) show the appearance of a new signal at ~2980 cm^{-1} assigned to H-bonded hydroxyl groups (O-H),[61] which was intensified over the subsequent OER processes (LSV10 - CA3). Notably, stretching vibration of the M-OOH was observed after CA1, evidenced by an increasing peak at ~1020 cm^{-1},[62,63] indicating its critical role as an active substance responsible for the progressively enhanced OER electrocatalysis.[64,65] Complementing these findings, the Raman peaks ascribed to Co-O characteristic at 404 cm^{-1}[30] gradually diminished (Fresh - LSV10). Instead, the new peaks at 456 and 508 cm^{-1} became increasingly pronounced as the OER processes progressed stepwise (CA1 - CA3), which are associated with the stretching vibrations of Co-OOH.[66–68] In addition, the W-O-W vibrational mode at 687 cm^{-1} underwent a red shift to a lower stretching frequency at 663 cm^{-1} after LSV5, attributed to the oxidized W valence state (SI, **Table S4**), and resulting modified electronic structure and W-O interaction strength.[69] Based on these findings, we propose that the remarkable self-optimization behavior is likely attributable to the in situ formation of OER-active Co-OOH species on the CuO substrate during OER electrocatalysis in alkaline media, accompanied by modifications in the electronic structure of W oxide with higher oxidation state.

To assess the potential decomposition of composite **3** and leakage of its components, ICP-OES analysis was conducted on the electrolyte throughout the stepped CA measurements. The analysis revealed that the concentrations of constituent metals (Co, W, and Cu) were below detectable limits, indicative of no metal leakage. These results underscore the exceptional mechanical stability of composite **3** during the progressively self-optimizing process, despite significant chemical adaptations occurring at the electrocatalyst interface under harsh oxidative and alkaline conditions.

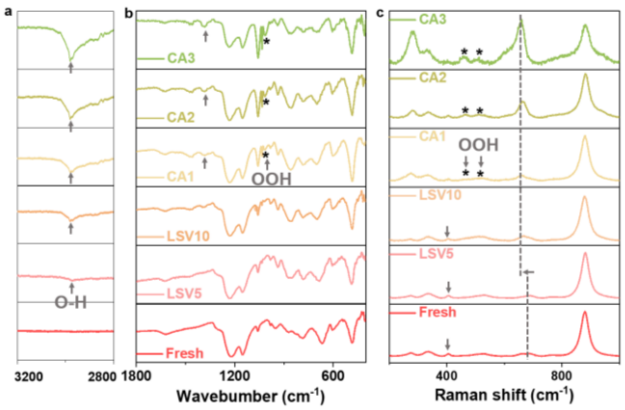

Fig. 4 OER process-dependent ATR-FTIR (a, b) and Raman (c) spectra of composite **3**.

Theoretical calculations:

In addition to the aforementioned insights at the molecular level, DFT calculations were performed to shed light on the catalytic mechanism of composite **3** at the atomic level. Building on the experimental XRD, TEM, XPS and ICP-OES data, two surface models, namely, as-prepared **3** and activated **3** after CA3 (**Fig. S30**), were established based on ab initio molecular dynamics (AIMD) calculation. Notably, the activated **3** after CA3 surface model incorporates additional oxygen atoms to replicate the chemical adaptation, e.g., in oxidation states and elemental ratios.

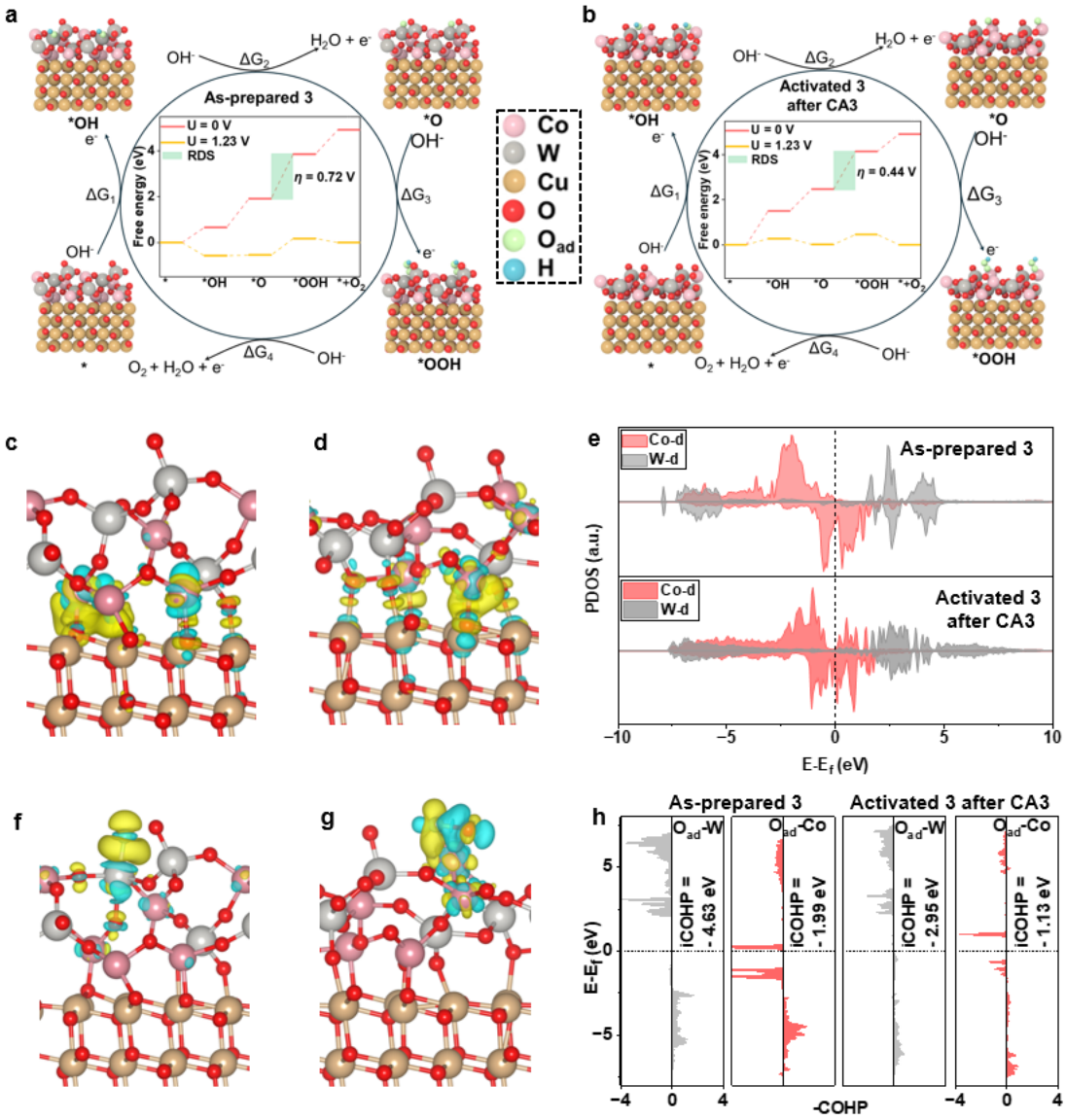

Fig. 5 DFT calculations on intrinsic mechanism. Schematic of the whole OER mechanism on as-prepared **3** (a) and activated **3** after CA3 (b) in the alkaline electrolyte. The inset shows the free energy profile at U = 0 V and U = 1.23 V. Difference charge density of as-prepared **3** (c) and activated **3** after CA3 (d). Yellow and cyan regions represent the increase and decrease of electron density, respectively. The iso-surfaces are plotted at the value of ± 0.006 |e|Å^{-3}. (e) Projected density of states (PDOS) of d-orbitals for the as-prepared **3** and activated **3** after CA3. Difference charge density diagrams of as-prepared **3** (f) and activated **3** after CA3 (g) after O adsorption on the surface. (h) Crystal orbital Hamilton population (COHP) analyses of O_{ad}-W and O_{ad}-Co bonds of as-prepared **3** and activated **3** after CA3.

Explicitly, we simulated the adsorption configurations of the reaction intermediates and the OER Gibbs free energy profiles at U = 0 V and U = 1.23 V, respectively. As evidenced by **Fig. 5a**, all the oxygen-containing intermediates (*OH, *O and *OOH) adsorbed on the W site of the as-prepared **3** surfaces, indicative of its preliminary role as the reactive site. Interestingly, for the activated **3** after CA3, the oxygen-containing intermediates (*OH, *O and *OOH) tended to adsorb on the Co site (**Fig. 5b**), which is considered to be the new active site responsible for the enhanced OER performance. Despite the adaptation of adsorption sites, the OER energy profile of both confirmed that the formation of *OOH intermediate from *O is the rate-determining step that overcame the highest energy barrier, which was matched well with the experimental ATR-FTIR and Raman spectroscopy results (**Fig. 4**). Correspondingly, the calculated OER overpotentials (η) for the as-prepared **3** is 0.72 V, while it is 0.44 V for the

activated **3** after CA3, which is lower than the calculated overpotential of 0.66 V for the commercial IrO_2.[70] This theoretical finding is in excellent agreement with the self-optimizing electrochemical performance observed (**Fig. 3i**). Additionally, the difference charge density diagrams show that significant charge transfer occurs at the interface between the deposited Co-W oxide and CuO substrate. In comparison to the as-prepared **3** (**Fig. 5c**), the electron transfer on the interfaces of the activated **3** after CA3 is more homogeneous and pronounced (**Fig. 5d**). Furthermore, the projected density of states (PDOS) was analyzed (**Fig. 5e**) to investigate the electronic properties of the two surfaces. The relative increase in DOS near the Fermi level for the activated **3** after CA3 renders more efficient interactions with the surrounding electrons, complementarily proving the aforementioned enhanced electrical conductivity (displayed in **Fig. 3h**) and therefore significantly boosting OER performance.[71]

To investigate the underlying self-activation mechanism for OER, we calculated the difference charge density for adsorbed O atom (O_{ad}) on the as-prepared **3** (**Fig. 5f**) and activated **3** after CA3 (**Fig. 5g**) surfaces. Notably, both of them feature considerable charge transfer, and the Bader charge results indicate that the charge transfer of the O_{ad} bound to W site of as-prepared **3** gains 0.88 e, while the O_{ad} bound to Co site of activated **3** after CA3 gains 0.31 e. Next, the crystal orbital Hamilton population (COHP) calculations were performed under O_{ad}-W or O_{ad}-Co bonding environments, respectively. Note that, the adsorption energies of O_{ad} on the W site and the Co site of as-prepared **3** are -3.62 eV and -2.98 eV (**Fig. 31**), while on the activated **3** after CA3 surface are -2.88 eV and -3.07 eV **(Fig. 32)**. Here, the energy value after integration up to the Fermi level (iCOHP) is an effective indicator of the bonding strength, where more negative iCOHP stands for higher bond energy, namely, stronger interaction.[72] As shown in Fig. **5h**, the iCOHP values of O_{ad}-W and O_{ad}-Co of as-prepared **3** are −4.63 eV and −1.99 eV, while they are −2.95 eV and -1.13 eV for the activated **3** after CA3, indicating stronger interactions between O_{ad}-W and O_{ad}-Co in the initial stage of the OER process. Consequently, a largeramount of O_{ad} atoms were attracted to the W sites due to the higher iCOHP value. After the self-activation process is finished (after CA3), the adsorption is weakened thanks to the O_{ad} atoms incorporation. In this context, the bond strength of O_{ad}-Co is moderate, and Co sites serve as reactive sites, contributing to the optimized OER catalytic activity.

Conclusion

In summary, we have successfully developed highly nanostructured mixed metal oxides based on the lab-synthesizable substrate, accessible using a facile wet-chemical deposition strategy. The resulting composite electrocatalyst presents unique self-optimizing behavior, leading to substantially improved OER performance metrics. Vibrational spectroscopic methods and DFT calculations unravel the dynamic adsorption site of involved intermediates and the nature of true active sites. This work provided essential experimental and theoretical insights into the self-optimization mechanism of multicomponent composite catalysts and offered a promising approach for the development of robust electrocatalysts for industrial alkaline OER.

Acknowledgments

Johannes Gutenberg University Mainz is gratefully acknowledged for financial support. D.G. acknowledges the Deutsche Forschungsgemeinschaft (DFG) for a Walter Benjamin Fellowship (project no. 510966757). C. N. and D.G. gratefully acknowledge the financial support by the Carl Zeiss Foundation (Halocycles no P2021-10-007). R.L., D. A. and B. F. M. acknowledge the Alexander-von-Humboldt-Foundation for a postdoctoral fellowship (project no. 1186323, 1235340 and 1231127, respectively). R.L. and D.G. gratefully acknowledge funding from the Top Level Research Area SusInnoScience of the federal state of Rheinland-Pfalz. The DFG for SFB1548 (project no. 463184206) is acknowledged for experimental support and TEM access.

Conflict of interest

The authors declare no conflict of interest.

References

[1] Z. P. Ifkovits, J. M. Evans, M. C. Meier, K. M. Papadantonakis, N. S. Lewis, *Energy Environ. Sci.* **2021**, *14*, 4740–4759.

[2] P. Lamers, T. Ghosh, S. Upasani, R. Sacchi, V. Daioglou, *Environ. Sci. Technol.* **2023**, *57*, 2464–2473.

[3] Z. Y. Yu, Y. Duan, X. Y. Feng, X. Yu, M. R. Gao, S. H. Yu, *Adv. Mater.* **2021**, *33*, 1–35.

[4] B. F. Mohazzab, K. Torabi, D. Gao, *Sustain. Energy Fuels* **2024**, Advance Article.

[5] H. Li, Y. Lin, J. Duan, Q. Wen, Y. Liu, T. Zhai, *Chem. Soc. Rev.* **2024**, *53*, 10709–10740.

[6] S. Cherevko, S. Geiger, O. Kasian, N. Kulyk, J. P. Grote, A. Savan, B. R. Shrestha, S. Merzlikin, B. Breitbach, A. Ludwig, et al., *Catal. Today* **2016**, *262*, 170–180.

[7] T. Naito, T. Shinagawa, T. Nishimoto, K. Takanabe, *Inorg. Chem. Front.* **2021**, *8*, 2900–2917.

[8] Z. Ma, Y. Zhang, S. Liu, W. Xu, L. Wu, Y. C. Hsieh, P. Liu, Y. Zhu, K. Sasaki, J. N. Renner, et al., *J. Electroanal. Chem.* **2018**, *819*, 296–305.

[9] Y. C. Zhang, C. Han, J. Gao, L. Pan, J. Wu, X. D. Zhu, J. J. Zou, *ACS Catal.* **2021**, *11*, 12485–12509.

[10] Y. Li, Y. Deng, D. Liu, Q. Ji, X. Cai, *Mater. Chem. Front.* **2023**, *8*, 880–902.

[11] M. Yu, E. Budiyanto, H. Tüysüz, *Angew. Chemie - Int. Ed.* **2022**, *61*, e202103824.

[12] X. Chen, J. Yang, Y. Cao, L. Kong, J. Huang, *ChemElectroChem* **2021**, *8*, 4427–4440.

[13] T. H. Wondimu, A. W. Bayeh, D. M. Kabtamu, Q. Xu, P. Leung, A. A. Shah, *Int. J. Hydrogen Energy* **2022**, *47*, 20378–20397.

[14] C. Xiao, Y. Li, X. Lu, C. Zhao, *Adv. Funct. Mater.* **2016**, *26*, 3515–3523.

[15] S. Jung, C. C. L. McCrory, I. M. Ferrer, J. C. Peters, T. F. Jaramillo, *J. Mater. Chem. A* **2016**, *4*, 3068–3076.

[16] F. Waag, B. Gökce, C. Kalapu, G. Bendt, S. Salamon, J. Landers, U. Hagemann, M. Heidelmann, S. Schulz, H. Wende, et al., *Sci. Rep.* **2017**, *7*, 1–13.

[17] D. Gao, R. Liu, S. Liu, S. Greiner, M. Anjass, J. Biskupek, U. Kaiser, H. Braun, T. Jacob, C. Streb, *ACS Appl. Mater. Interfaces* **2021**, *13*, 19048–19054.

[18] M. Kuang, P. Han, Q. Wang, J. Li, G. Zheng, *Adv. Funct. Mater.* **2016**, *26*, 8555–8561.

[19] T. Chen, H. Ren, L. Li, W. Tan, H. He, *Mater. Chem. Phys.* **2024**, *313*, 128689.

[20] J. Ahmed, N. Alhokbany, T. Ahamad, S. M. Alshehri, *New J. Chem.* **2022**, *46*, 1267–1272.

[21] X. Yue, Y. Zheng, Y. Chen, S. Huang, *Electrochim. Acta* **2020**, *333*, 135554.

[22] Z. Xi, A. Mendoza-Garcia, H. Zhu, M. F. Chi, D. Su, D. P. Erdosy, J. Li, S. Sun, *Green Energy Environ.* **2017**, *2*, 119–123.

[23] Z. L. Wang, K. A. Wang, X. Xiao, H. Bin Zhu, *Chem. Eng. J.* **2024**, *496*, 154218.

[24] R. Gong, D. Gao, R. Liu, D. Sorsche, J. Biskupek, U. Kaiser, S. Rau, C. Streb, *ACS Appl. Energy Mater.* **2021**, *4*, 12671–12676.

[25] Z. N. Zahran, E. A. Mohamed, Y. Tsubonouchi, M. Ishizaki, T. Togashi, M. Kurihara, K. Saito, T. Yui, M. Yagi, *ACS Appl. Energy Mater.* **2021**, *4*, 1410–1420.

[26] S. Si, H. S. Hu, R. J. Liu, Z. X. Xu, C. Bin Wang, Y. Y. Feng, *Int. J. Hydrogen Energy* **2020**, *45*, 9368–9379.

[27] W. Luo, J. Hu, H. Diao, B. Schwarz, C. Streb, Y. F. Song, *Angew. Chem. Int. Ed.* **2017**, *56*, 4941–4944.

[28] M. Nakayama, A. Takeda, H. Maruyama, V. Kumbhar, O. Crosnier, *Electrochem. commun.* **2020**, *120*, 106834.

[29] N. Krishankant, N. Aashi, Z. Ahmed, S. Alagar, A. Gaur, R. Kaur, V. Bagchi, *Sustain. Energy Fuels* **2022**, *6*, 4429–4436.

[30] D. Gao, R. Liu, J. Biskupek, U. Kaiser, Y. F. Song, C. Streb, *Angew. Chem. Int. Ed.* **2019**, *58*, 4644–4648.

[31] N. Gupta, C. Segre, C. Nickel, C. Streb, D. Gao, K. D. Glusac, *ACS Appl. Mater. Interfaces* **2024**, *16*, 35793–35804.

[32] P. He, X. Y. Yu, X. W. D. Lou, *Angew. Chemie - Int. Ed.* **2017**, *56*, 3897–3900.

[33] P. Zhang, X. F. Lu, J. Nai, S. Q. Zang, X. W. Lou, *Adv. Sci.* **2019**, *6*, 1–7.

[34] Y. Li, C. Zhao, *Chem. Mater.* **2016**, *28*, 5659–5666.

[35] T. Kang, K. Kim, M. Kim, J. Kim, *J. Catal.* **2021**, *404*, 80–88.

[36] X. Zhang, L. Zhang, Y. Zhu, Z. Li, Y. Wang, T. Wågberg, G. Hu, *ChemSusChem* **2021**, *14*, 467–478.

[37] I. Yamada, M. Kinoshita, S. Oda, H. Tsukasaki, S. Kawaguchi, K. Oka, S. Mori, H. Ikeno, S. Yagi, *Chem. Mater.* **2020**, *32*, 3893–3903.

[38] L. N. Nguyen, U. T. D. Thuy, Q. D. Truong, I. Honma, Q. L. Nguyen, P. D. Tran, *Chem. - An Asian J.* **2018**, *13*, 1530–1534.

[39] R. Gong, D. Gao, R. Liu, D. Sorsche, J. Biskupek, U. Kaiser, S. Rau, C. Streb, *ACS Appl. Energy Mater.* **2021**, *4*, 12671–12676.

[40] J. Zhang, Q. Zhang, X. Feng, *Adv. Mater.* **2019**, *31*, 1–19.

[41] K. J. Lee, N. Elgrishi, B. Kandemir, J. L. Dempsey, *Nat. Rev. Chem.* **2017**, *1*, 39.

[42] J. Li, J. Gong, *Energy Environ. Sci.* **2020**, *13*, 3748–3779.

[43] H. Xu, H. Shang, C. Wang, Y. Du, *Coord. Chem. Rev.* **2020**, *418*, 213374.

[44] D. Gao, S. Liu, R. Liu, C. Streb, *Chem. Eur. J.* **2020**, *26*, 11109-11112.

[45] Y. Du, X. Gao, X. Meng, *Phys. B Condens. Matter* **2019**, *560*, 37–40.

[46] Y. Deng, A. D. Handoko, Y. Du, S. Xi, B. S. Yeo, *ACS Catal.* **2016**, *6*, 2473–2481.

[47] P. Muthukumar, M. Pannipara, A. G. Al-Sehemi, S. P. Anthony, *New J. Chem.* **2020**, *44*, 11993–12001.

[48] S. Corby, L. Francàs, A. Kafizas, J. R. Durrant, *Chem. Sci.* **2020**, *11*, 2907–2914.

[49] Y. Li, Y. Wang, J. Lin, Y. Shi, K. Zhu, Y. Xing, X. Li, Y. Jia, X. Zhang, *Front. Energy Res.* **2022**, *10*, 1–9.

[50] M. C. Biesinger, *Surf. Interface Anal.* **2017**, *49*, 1325–1334.

[51] Y. Shimoyama, N. Ogiwara, Z. Weng, S. Uchida, *J. Am. Chem. Soc.* **2022**, *144*, 2980–2986.

[52] F. Jafari, M. B. Gholivand, *Mater. Today Chem.* **2023**, *29*, 101432.

[53] W. Iqbal, M. Mekki, W. Rehman, B. Shahzad, U. Anwar, S. Mahmood, M. E. Talukder, *Dig. J. Nanomater. Biostructures* **2023**, *18*, 403–410.

[54] C. Yang, C. Wöll, *Adv. Phys. X* **2017**, *2*, 373–408.

[55] X. Xiao, R. Ma, D. Li, M. Yang, Y. Tong, Z. Qiu, B. Jing, T. Yang, R. Hu, Y. Yang, et al., *J. Alloys Compd.* **2023**, *968*, 171910.

[56] Y. Deng, A. D. Handoko, Y. Du, S. Xi, B. S. Yeo, *ACS Catal.* **2016**, *6*, 2473–2481.

[57] C. Luan, J. Angona, A. Bala Krishnan, M. Corva, P. Hosseini, M. Heidelmann, U. Hagemann, E. Batsa Tetteh, W. Schuhmann, K. Tschulik, et al., *Angew. Chemie - Int. Ed.* **2023**, *62*, e202305982.

[58] L. Yang, L. Zhang, Y. Li, B. H. Lee, J. Kim, H. S. Lee, J. Bok, Y. Ma, W. Zhou, D. Yuan, et al., *J. Am. Chem. Soc.* **2024**, *146*, 12556–12564.

[59] Y. C. Zhang, M. Zhao, J. Wu, Y. Wang, L. Zheng, F. Gu, J. J. Zou, J. Gao, X. D. Zhu, *ACS Catal.* **2024**, *14*, 7867–7876.

[60] X. Gao, Y. Yu, Q. Liang, Y. Pang, L. Miao, X. Liu, Z. Kou, J. He, S. J. Pennycook, S. Mu, et al., *Appl. Catal. B Environ.* **2020**, *270*, 118889.

[61] A. D. Jagadale, D. P. Dubal, C. D. Lokhande, *Mater. Res. Bull.* **2012**, *47*, 672–676.

[62] Y. Lin, Z. Liu, L. Yu, G. R. Zhang, H. Tan, K. H. Wu, F. Song, A. K. Mechler, P. P. M. Schleker, Q. Lu, et al., *Angew. Chemie - Int. Ed.* **2021**, *60*, 3299–3306.

[63] Q. Ji, Y. Kong, H. Tan, H. Duan, N. Li, B. Tang, Y. Wang, S. Feng, L. Lv, C. Wang, et al., *ACS Catal.* **2022**, *12*, 4318–4326.

[64] M. Retuerto, L. Pascual, J. Torrero, M. A. Salam, Á. Tolosana-Moranchel, D. Gianolio, P. Ferrer, P. Kayser, V. Wilke, S. Stiber, et al., *Nat. Commun.* **2022**, *13*, 7935.

[65] F. Song, L. Bai, A. Moysiadou, S. Lee, C. Hu, L. Liardet, X. Hu, *J. Am. Chem. Soc.* **2018**, *140*, 7748–7759.

[66] M. Wang, Q. Wa, X. Bai, Z. He, W. S. Samarakoon, Q. Ma, Y. Du, Y. Chen, H. Zhou, Y. Liu, et al., *JACS Au* **2021**, *1*, 2216–2223.

[67] H. Jia, N. Yao, Z. Liao, L. Wu, J. Zhu, Y. Lao, W. Luo, *Angew. Chemie Int. Ed.* **2024**, *63*, e202408005.

[68] Y. Chen, Z. Yu, R. Jiang, J. Huang, Y. Hou, J. Chen, Y. Zhang, H. Zhu, B. Wang, M. Wang, *Small* **2021**, *17*, 1–13.

[69] E. Cazzanelli, C. Vinegoni, G. Mariotto, A. Kuzmin, J. Purans, *Solid State Ionics* **1999**, *123*, 67–74.

[70] F. Liao, K. Yin, Y. Ji, W. Zhu, Z. Fan, Y. Li, J. Zhong, M. Shao, Z. Kang, Q. Shao, *Nat. Commun.* **2023**, *14*, 1248.

[71] R. Urrego-Ortiz, S. Builes, F. Calle-Vallejo, *ACS Catal.* **2022**, *12*, 4784–4791.

[72] Q. Liu, L. Yang, Z. Mei, Q. An, K. Zeng, W. Huang, S. Wang, Y. Sun, H. Guo, *Energy Environ. Sci.* **2024**, *17*, 780–790.